AIAA SciTech Forum
January 3-7, 2022, San Diego, CA & Virtual
AIAA SCITECH 2022 Forum

10.2514/6.2022-2048

Investigation of Ammonia-Hydrogen Mixture as a Green Fuel for Jet Engines Using a Wave Reformer

Pejman Akbari[1]
California State Polytechnic University
Pomona, CA, 91768,
USA

Colin D. Copeland[2]
Simon Fraser University
Vancouver, BC, V3T 4B7,
Canada

Stefan Tüchler[3]
New Wave Hydrogen Inc.,
Canada

Alison M. Ferris[4]
Stanford University,
Stanford, CA 94305, USA

David F. Davidson[5]
Stanford University,
Stanford, CA 94305, USA

Ronald K. Hanson[6]
Stanford University,
Stanford, CA 94305, USA

This paper explores the idea of thermally cracking ammonia via shock waves to produce a blend of ammonia-hydrogen as a 'carbon neutral' aviation fuel, reducing global carbon dioxide emissions. The method is based on wave rotor technology utilizing the energy contained in the combustor burned gas to compress and heat ammonia to temperatures at which high conversion rates can be achieved on short timescales. Then, the resulting ammonia-hydrogen mixture is fed into the burner as reactant which leads to hydrogen, nitrogen, and water vapor as primary gas products. The shock wave process has been modeled numerically using an in-house quasi-one-dimensional code by Tüchler and Copeland that has been experimentally validated for non-reacting wave rotors. A single-reaction, global kinetic model was developed to approximate the NH_3 pyrolysis reaction chemistry across the temperature and pressure conditions of interest, thereby enabling the incorporation of chemistry in the numerical simulations. The computational results provide data used in the prediction of flow fields inside the channels of the wave reformer and at the inflow/outflow ports of the reactor. The data confirm production of a mixture of ammonia and hydrogen using energy harvested from the engine burner exhaust. This study introduces a new application of the shock-wave reforming process as well as another step in the realization of ammonia as an aviation fuel without carbon content.

I. Introduction

The evidence of environmental damage caused by consumption of carbon-based fossil fuels is overwhelming. The aviation sector is among important transportation segments that contribute to environmental emissions and deterioration. While the aviation industry primarily utilizes petroleum-based fuels, hydrogen and ammonia offer interesting pathways for achieving sustainable and green aviation. Both fuels have been extensively explored as alternative fuels in ground vehicles and gas turbine engines [1].

The potential of using hydrogen fuel for a jet engine as a long-term energy solution has received significant attention recently [2]. As a clean fuel, combustion of hydrogen with air does not release any harmful, carbon-containing green-house gases contributing to global warming. Additionally, (liquid) hydrogen contains 2.8 times more energy than conventional aircraft kerosene fuel [3]. Ammonia, as another zero-carbon fuel, offers an energy density

---

[1] Associate Professor, Electromechanical Engineering Department, AIAA Member.
[2] Associate Professor, School of Sustainable Energy Engineering.
[3] Research Associate, Mechanical Engineering Department.
[4] Research Scientist, Mechanical Engineering Department, AIAA Member.
[5] Senior Research Engineer, Mechanical Engineering Department, AIAA Member.
[6] Professor, Mechanical Engineering Department, AIAA Fellow.

even higher than compressed hydrogen [4]. It can be easily stored in relatively low-pressure tanks (e.g., pressure of 8.8 atm at 21^0C). Ammonia is also a well-known hydrogen carrier, thus, producing hydrogen from ammonia is also possible.

Even though these carbon-free fuels have the potential to replace hydrocarbon fuels, there are a number of barriers that must be overcome before such fuels can be commercially used for both transport and power applications. For instance, the use of hydrogen is compromised by the fact that the space required to store liquid hydrogen is 4 times the volume needed to store kerosene; due to its lower density. This introduces significant challenges associated with the design of fuel tanks for airborne applications. Meanwhile, high NO_x emissions associated with ammonia oxidation [5], along with its low flame speed [6], have hindered the use of ammonia as a sustainable fuel in aviation. Results have shown positive power production, but this power production comes at a cost of high NO_x emissions due to the N atom in ammonia molecules that is not present in conventional hydrocarbon fuels [7]. The NO_x emissions challenge for ammonia-fueled turbine engines has been recognized as one the of main limitations of this fuel [1-6, 8]. New findings show that addition of hydrogen can improve flame stability and reduce NO_x emissions [9]. In addition, co-combustion of ammonia and hydrogen has been shown to enhance the flame speed [10]. These results encourage further tests and research for deployment of ammonia-based propulsion systems.

Here, a new pyrolysis method is proposed that uses a wave-rotor reformer to generate and provide a zero-carbon fuel blend of ammonia and hydrogen on a continuous basis, benefiting from both fuels and effectively reducing emissions. Although wave rotor technology has already been shown to enhance the performance of aircraft engines [11, 12], this work illustrates a completely new application of wave rotors to produce gaseous ammonia-hydrogen fuel blend that can be used for aviation or for power-generation applications. This study will describe how a wave-rotor reformer uses shock waves to compress preheated ammonia by direct utilization of the energy from hot, high-pressure combustion products. The shock-compression raises the ammonia temperature sufficiently high to achieve thermal decomposition and the partial cracking of ammonia into hydrogen, thereby resulting in a zero-carbon, ammonia-hydrogen fuel mixture for a burner of an engine, fuel mixture for a burner of an engine.

New Wave Hydrogen, Inc. (New Wave H_2 or NWH_2) has recently introduced a rotary wave reformer using the wave rotor technology for methane-pyrolysis processing [13, 14]. The goal is to achieve a rapid and homogeneous temperature amplification sufficient to thermally decompose (i.e., crack) hydrocarbons entering the rotor channels. The shock heating splits methane into hydrogen and solid carbon in the absence of oxygen, i.e., $CH_4 \rightarrow C + 1.5\ H_2$. A main characteristic of this process is the absence of oxygen, which eliminates CO_2 and CO by-products. This is an important distinction relative to competing methods of methane pyrolysis, i.e., the gas is not heated using electrical or plasma powered sources, it is heated by the rapid compression wave cycle. More details can be found in the references above.

It is now envisioned to use the rotary wave reforming concept to compress and heat ammonia until it breaks apart into its constituent species (i.e., $NH_3 \rightarrow 0.5\ N_2 + 1.5\ H_2$). This is an endothermic reaction requiring 46 KJ/mol_{NH3} which can be provided by a hot, high-pressure driver gas source. The wave reformer benefits from energy transfer in the shock wave and the use of the energy embodied in the burned gas. With regard to ammonia reforming onboard a wave reformer, the process is equivalent to ammonia thermal cracking using shock waves in a shock tube. Ammonia thermal decomposition using shock waves has been demonstrated in previous shock tube studies [15-17]. By adjusting the rotor speed, channel length, and optimizing port arrangements, it is possible to thermally crack ammonia in a wave reformer on timescales similar to those seen in a shock tube.

II. Pyrolysis of Ammonia by Shock Waves

The combustion kinetics of ammonia has been the focus of many research activities, due to the high potential of ammonia as a fuel for internal combustion engines as well as gas turbines [4, 5]. Many studies on the combustion properties of ammonia-air or ammonia-oxygen mixtures utilizing shock heating in shock tubes have been reported [18-20], but only a select few studies have been conducted to characterize the decomposition of ammonia in the absence of air/oxygen [15-17]. To verify formation of hydrogen through shock-heating of ammonia, numerical modeling was first conducted to simulate dissociation of ammonia in a conventional shock tube.

A. Chemical Kinetic Modeling

A single-step, global reaction mechanism was developed to facilitate efficient, realistic modeling of the shock-wave reforming process. Ammonia pyrolysis is a complex, multi-step mechanism [16] and development of detailed chemical kinetic models to accurately describe the pyrolysis of ammonia is an active area of study (e.g., [15]). In the current work, we seek to leverage existing knowledge of ammonia pyrolysis reaction pathways to identify a single-step, three-species, global reaction mechanism that can be used in the place of a detailed model, thereby reducing computational complexity and time.

First, a detailed chemical kinetic model developed by Glarborg et al. [21] was used in conjunction with the Chemkin-PRO (ANSYS, Inc. [22]) software package to simulate ammonia pyrolysis at temperatures and pressures representative of post-reflected shock conditions in a wave reformer (i.e., six conditions across 1900-2300 K and 70-80 atm – see Section IV). The system was simulated as a 0-D, constant-enthalpy, constant-pressure (constant-HP) reactor; the reactant was assumed to be 100% NH_3; and the simulated test time was 5 milliseconds (the wave reformer residence time, post-reflected shock, is estimated to be approximately 4 milliseconds). The modeled NH_3 and H_2 species time-histories are plotted in Fig. 1.

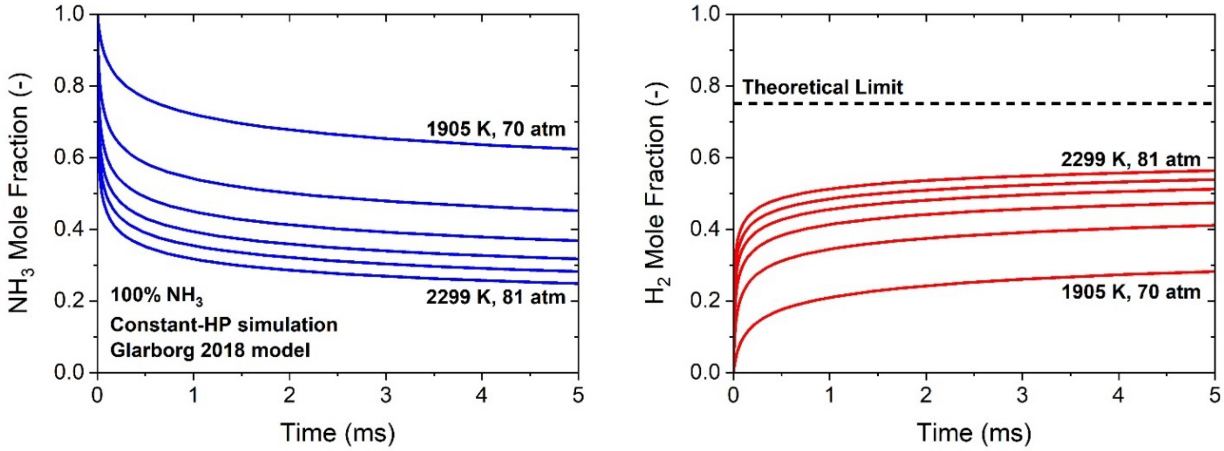

Figure 1: Estimated NH_3 (left) and H_2 (right) time-histories at six conditions of interest, simulated using a detailed kinetic model developed by Glarborg et al. **[**21**]**. Theoretical limit designates the expected H_2 mole fraction if 100% of the hydrogen contained in NH_3 was converted to H_2.

At the lowest temperature and pressure condition (1905 K, 70 atm), nearly 40% NH_3 conversion is achieved after 5 milliseconds; at the highest temperature and pressure condition (2299 K, 81 atm), approximately 75% NH_3 conversion is achieved after 5 milliseconds. As expected, NH_3 decomposition correlates with H_2 formation: at the highest temperature and pressure condition, the most H_2 is formed, approaching nearly 60% mole fraction after 5 milliseconds. The wide range of NH_3 conversion efficiencies observed across the six conditions is encouraging, as it indicates this process could be used to generate NH_3/H_2 mixtures with varied NH_3-to-H_2 ratios; a specific NH_3-to-H_2 ratio in this range could be desired for optimal combustion behavior, for example.

Reaction pathway analysis of the Glarborg et al. [21] model confirms that ammonia pyrolysis is primarily dominated by the following reactions:

$$NH_3 = NH_2 + H \qquad \text{(R1)}$$

$$NH_3 + H = NH_2 + H_2 \qquad \text{(R2)}$$

$$NH_2 + NH_2 = \text{various products} \qquad \text{(R3)}$$

Here, R1 serves as an initial unimolecular decomposition step, R2 is a propagation step characterized by ammonia attack by H-atoms, and R3 is a propagation step responsible for the formation of intermediate species that eventually degrade to H_2 and N_2. Closer inspection of the intermediate species formed during NH_3 pyrolysis confirms this observation. Figure 2 shows the estimated species time-histories of the 10 most significant species formed during NH_3 pyrolysis at 2211 K, 80 atm, simulated using the Glarborg et al. kinetic model.

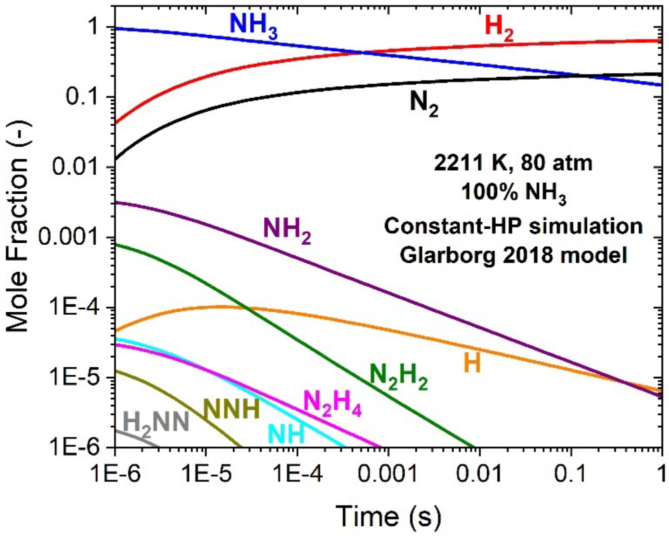

Figure 2: Simulated intermediate and final species formed during the pyrolysis of 100% NH_3 at 2211 K, 80 atm; simulated using a detailed kinetic model developed by Glarborg et al. **[**21**]**.

As can be seen in Fig. 2, significant amounts of NH_2 and N_2H_2 are formed within the first microsecond. However, these species are soon consumed, dropping 1-2 orders of magnitude by 1 millisecond. The significant presence of these intermediate species at early times suggests this pyrolysis system cannot be modeled accurately across the entire time domain using a single, global reaction. However, the trends in Fig. 2 also show that at late times (e.g., time > 1 millisecond), the intermediate species no longer play an important role.

The following one-step reaction was chosen to approximate the thermal decomposition of NH_3 to H_2 and N_2 at late times:

$$2NH_3 \rightarrow 3H_2 + N_2 \qquad \text{(R4)}$$

This reaction is assumed to take a standard Arrhenius form, where the bimolecular reaction rate, k_{R4}, is defined as:

$$k_{R4} = A \exp\left(-\frac{E_a}{RT}\right) \qquad (1)$$

Here, A is a pre-exponential factor, E_a is the activation energy, R is the ideal gas constant, and T is temperature.

A grid search was performed to determine the optimal pre-exponential A-factor and activation energy needed for the global, single-step reaction mechanism to approximate the simulation results generated using the full, detailed kinetic model of Glarborg et al. at times between 1.2 and 5 milliseconds. A wide range of E_a and A values was interrogated, and for each combination, a value for k was calculated and used to simulate time-resolved NH_3, H_2, and N_2 mole fractions at the six temperature and pressure conditions of interest. The H_2 mole fraction traces were then compared to the corresponding traces simulated using the detailed Glarborg et al. model, and a mean, relative difference between the two sets of results was calculated. The optimal values for A and E_a correspond to the values for which the mean relative difference between the two sets of model results is minimized. The results of this grid search can be seen in Fig. 3.

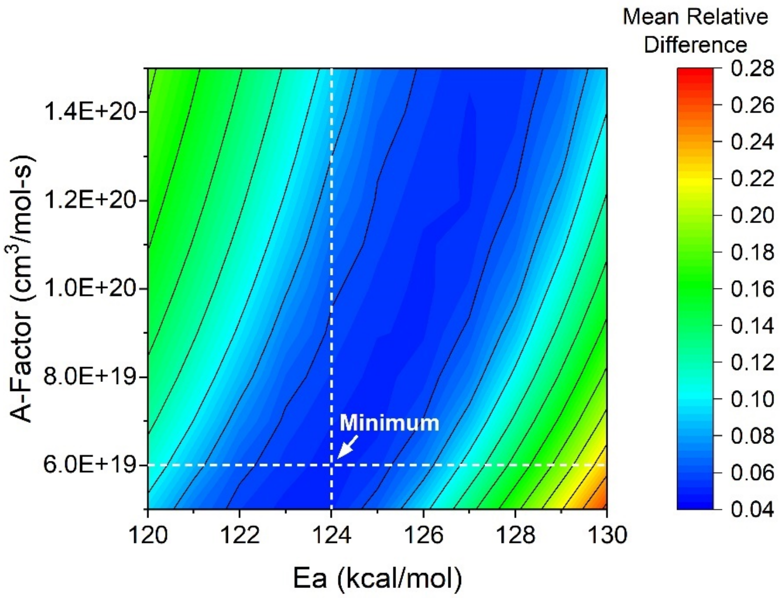

Figure 3. Results of grid search performed to identify the combination of *A* and E_a needed to minimize the mean, relative difference between H_2 mole fraction results simulated using our single-reaction model and the detailed model developed by Glarborg et al. **[**21**]**.

The optimal values for the pre-exponential *A*-factor and activation energy were found to be 6×10^{19} cm^3/mol-s and 124,000 cal/mol, respectively, yielding the following expression for k_{R4}:

$$k_{R4} = 6 \times 10^{19} \exp\left(-\frac{124000}{RT}\right) \quad \frac{cm^3}{mol \cdot s} \tag{2}$$

The performance of the optimized, single-reaction model is shown in Fig. 4.

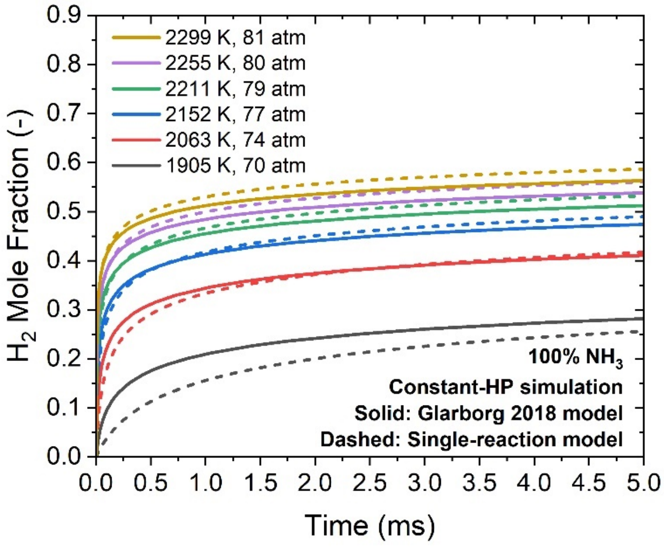

Figure 4: Simulated H_2 mole fraction results predicted using the optimized, single-reaction model, compared to the H_2 mole fraction results predicted using the detailed kinetic model of Glarborg et al.

As can be seen in Fig. 4, the single-reaction model closely captures the H_2 mole fraction trends predicted by the full, detailed kinetic model of Glarborg et al. At 4 milliseconds, the average relative difference between the H_2 mole fraction results simulated using the two modeling approaches was found to be 4.6%. The lowest relative difference at 4 milliseconds was observed in the 2063 K case (1.0%), and the highest relative difference at 4 milliseconds was observed in the 1905 K case (11.5%).

Overall, at the residence time of interest in this work (4 milliseconds), and across the temperature and pressure conditions of interest, the single-reaction mechanism is expected to approximate the results of a more detailed kinetic model within 1-11.5% and is expected to perform better at the higher temperature/pressure conditions.

B. Shock-Wave Heating

To investigate the influence of the driver gas initial temperature on shock heating, the one-dimensional Riemann or Sod shock-tube problem is considered. The problem represents an initial value problem (IVP) and is solved exactly assuming that the working medium behaves as an inviscid and calorically perfect gas.

The resulting *x-t* schematic shown in Fig. 5 outlines the wave patterns and respective states within the shock tube in a steady-state manner. This represents one particular solution to the IVP problem , where the driver gas (State 4) features a higher pressure than the driven section (State 1).

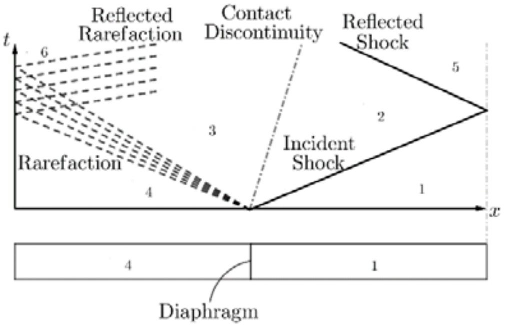

Figure 5: Wave propagation in a shock tube.

Solving the shock tube problem for a wide range of pressure ratios between the driver and driven sections, enables the computation of the subsequent temperature rises across incident and reflected shock waves. Figure 6 (left) shows the temperature rise across the incident shock wave (T_2 /T_1) as a function of pressure ratios in the shock tube (P_4 /P_1) by varying the driver gas initial temperature (T_4) in increments of 200 K from 1300 K to 2100 K. The pressure in the driven section is assumed to be at ambient conditions of 1 atm and 300 K. Both sections are initially at rest. It is seen that by increasing the driver gas initial temperature, greater temperature rise across the incident shock wave is obtained. Similarly, Fig. 6 (right) illustrates the temperature rise across the combination of the incident-reflected shock waves (T_5 /T_1) as a function of pressure ratio in the shock tube by varying the driver gas initial temperature. The behavior of this temperature rise is similar to that in Fig. 6 (left). It is seen that temperature rises beyond 3 can be attained for the pressure ratio above 30 in the shock tube, confirming the potential of shock heating to achieve sufficiently large temperatures to initiate ammonia cracking even with relatively moderate initial driver and driven temperatures provided the shock compression is sufficiently strong.

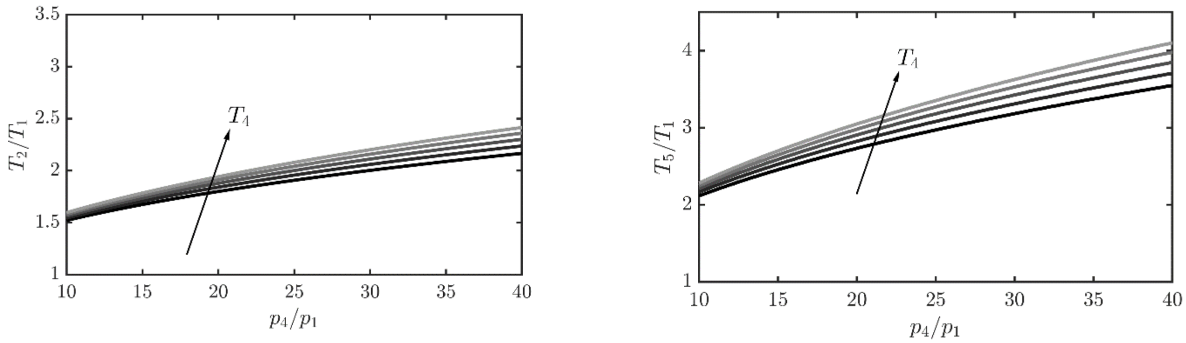

Figure 6: (Left) temperature rise across an incident shock wave, (Right) temperature rise across both incident and reflected shock waves as functions of pressure ratio between driver and driven sections and initial temperature of the driver gas.

C. Numerical Modeling of Ammonia Pyrolysis in a Shock Tube

The numerical tool used to predict ammonia pyrolysis in a shock tube is a quasi-one-dimensional wave rotor code developed and experimentally validated by Tüchler and Copeland at University of Bath, UK [23-25] for non-reacting wave rotors. The model solves the laminar one-dimensional Navier-Stokes equations using a two-step Richtmyer TVD scheme with minmod flux limiter. The code follows a single wave rotor passage of constant cross section as it passes ports along the circumference and accurately computes unsteady wave action in the rotor channels as well as steady conditions in the ports. To account for pyrolysis of reactants, the model has been modified to employ the simple, one-step reaction rate described in the previous section, which turns the reactant (ammonia) into products (e.g. hydrogen and nitrogen).

The equations are as follows:

$$\frac{\partial \vec{U}}{\partial t} + \frac{\partial \vec{F}}{\partial x} = \vec{S} \tag{3}$$

The state vector $\vec{U}$, flux vector $\vec{F}$ and source term vector $\vec{S}$ are:

$$\vec{U} = \begin{pmatrix} \rho \\ \rho u \\ \rho E \\ \rho Y_i \\ \vdots \\ \rho Y_n \end{pmatrix}, \qquad \vec{F} = \begin{pmatrix} \rho \\ \rho u \\ \rho E \\ \rho Y_i \\ \vdots \\ \rho Y_n \end{pmatrix}, \qquad \vec{S} = \begin{pmatrix} 0 \\ 0 \\ \dot{\omega}_T \\ \dot{\omega}_i \\ \vdots \\ \dot{\omega}_n \end{pmatrix} \tag{4}$$

Where ρ denotes the density of the mixture, u the velocity in x-direction, p the static pressure and E the total energy per unit volume. The quantity Y_i represents the mass fraction of each chemical species, while the source terms accounting for reaction contain the mass reaction rate $\dot{\omega}_i$ and the endothermic heat absorption $\dot{\omega}_T$.

The production rate and the heat absorption follow:

$$\dot{\omega} = \nu k_{R4} \rho Y \tag{5}$$

$$\dot{\omega}_T = -Q\dot{\omega} \tag{6}$$

where ν represents the stoichiometric coefficient and Q the heat absorption per unit mass of reactant.

In addition, the mass fraction and mass reaction rate satisfy the following equation:

$$\sum_{i=1}^{n} Y_i = 1, \sum_{i=1}^{n} \dot{\omega}_i = 0 \tag{7}$$

It is also assumed that each species follows the ideal gas law:

$$p = \rho RT \sum_{i=1}^{n} \frac{Y_i}{W_i} \tag{8}$$

with R used as the universal gas constant.

Hence, using the reactive quasi-one-dimensional model, a solution of the one-dimensional Riemann or Sod shock-tube problem for ammonia decomposition was studied as described in the following.

Referring to Fig. 5, in this study NH_3 at 1 atmosphere pressure and 400 K temperature was considered in the driven section (State 1), and N_2 at 38 atm and 2000 K in the driver section (State 4) was introduced. Both driver and driven gas are assumed to be at rest at the start of the simulation. The simulation ran for 15 milliseconds and the total shock tube length was chosen to be 2 m with the diaphragm located at the center (i.e., at x = 0 m). The rupture of the diaphragm generates a right-running incident shock wave followed by a contact discontinuity and a left-running expansion fan or rarefaction wave. The right-running incident shock wave changes NH_3 properties from State 1 to State 2. Meanwhile, the left-running expansion fan changes N_2 properties from State 4 to State 3. NH_3 properties behind the left-running reflected shock wave generated at the right wall are represented by State 5.

Figure 7 shows color contours of pressure, temperature, Mach number, and velocity in the shock tube, as functions of time, i.e. in the distance-time space. The horizontal axis of each contour represents non-dimensional distance along the tube (*x/L*). The vertical axis represents time. Due to the relatively high pressure differences between the driver and driven gases (i.e. $P_4 >> P_1$), the pressure contours are given in logarithmic form to enhance the visibility of shock and expansion waves. The pressure plot shows compression of NH_3 by both incident and reflected shock waves. In addition, the attenuation of the shock waves due to viscous effects can be seen as time progresses. The temperature plot indicates a temperature rise for NH_3 from its initial 400 K as expected through shock heating. However, the highest-temperature zone is not near to the right wall (e.g., State 5). In fact, the highest-temperature region is offset from the end wall, and starts at the contact surface separating the compressed NH_3 and the N_2 and continues in the hot N_2 region after the reflected shock wave travels to the left and compresses N_2. This is different from a typical shock tube where the driver and driven gases usually have equal or near-equal initial temperatures. The Mach number and velocity plots show the flow directions. The incident shock wave has induced a supersonic region in the post-shock gas.

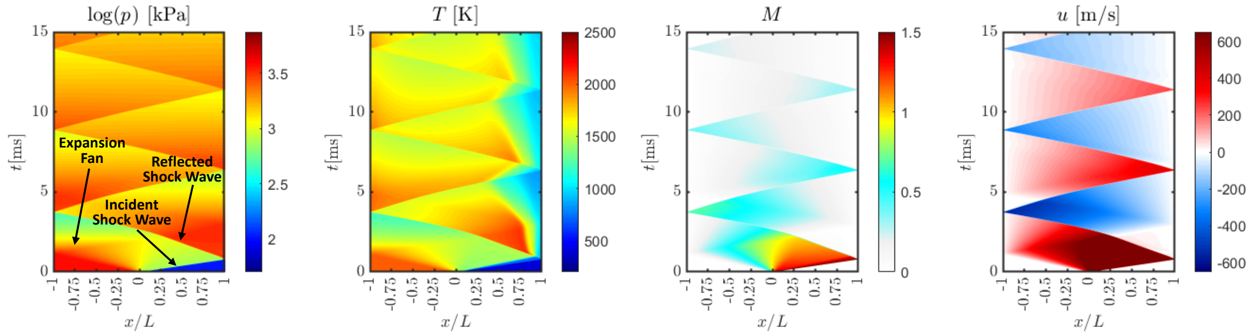

Figure 7: Contours of pressure, temperature, Mach number, and velocity in a shock tube as functions of time.

The species contours shown in Fig. 8 outline the temporal and spatial evolution of molar fractions for NH_3, N_2, and the resulting H_2. The NH_3 concentration plot shows the gas is pushed by the incident shock wave towards the right wall where it starts to partially decompose to N_2 and H_2. The N_2 concentration plot indicates the gas penetrates into the driven section of the tube, and after about 1 millisecond the (first) reflected shock wave stops the gas penetration. The H_2 concentration plot shows formation of hydrogen far away from the wall and near to the contact surface between the compressed NH_3 and the N_2. There is still some fuel-to-hydrogen conversion taking place next to the wall, but much less than further away from the wall.

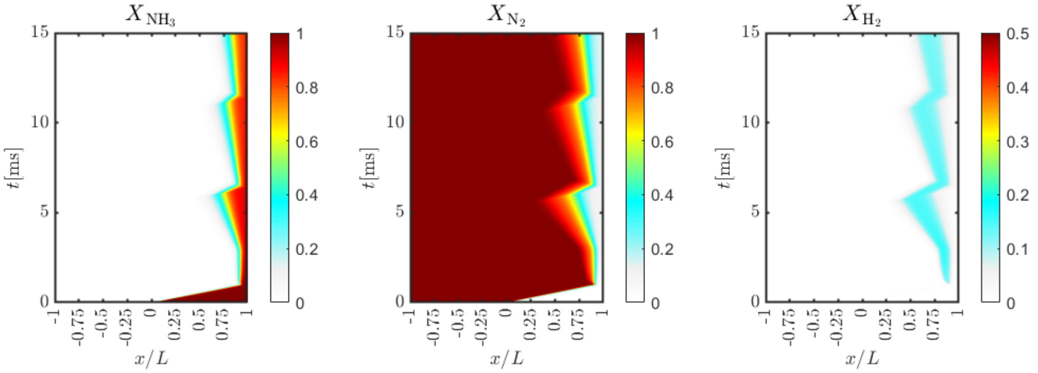

Figure 8: Mole fraction contours of NH_3 (left), N_2 (middle), and H_2 (right) in a shock tube as functions of time.

To show the temperature range of each species, Fig. 9 is presented where the temperature field for each species is shown. In this layout, the peak temperature of each species along with the location and time of its occurrence can be determined. For NH_3 (left) a maximum temperature up to 1700 K can be obtained, which is sufficient for ammonia decomposition. The N_2 (middle) temperature increases beyond 2000 K and the H_2 temperature exceeds 1800 K in some locations which is a temperature suitable for hydrogen production.

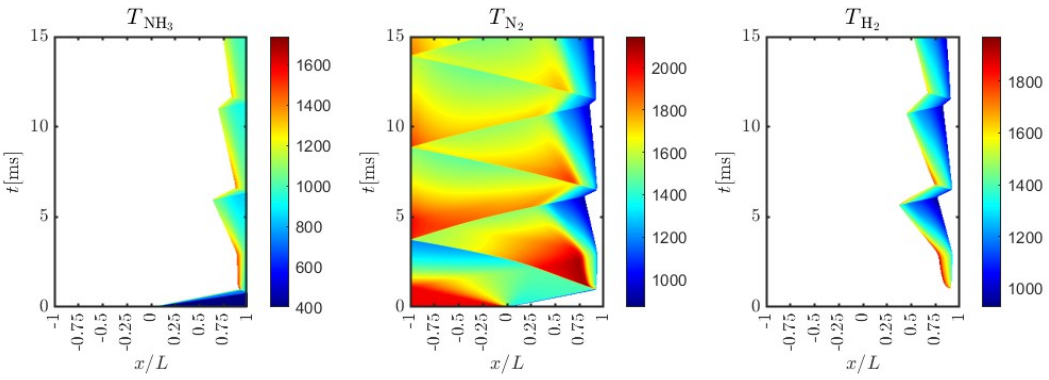

Figure 9: Temperature range for NH_3 (left), N_2 (middle), and H_2 (right) in shock tube as functions of time.

To explore the impact of the temperature drop due to the endothermic effect on H_2 production, Fig. 10 is presented which predicts the difference in hydrogen molar fraction produced with and without the endothermic effect. This was achieved by setting the heat source term accounting for the endothermic heat absorption to zero. The plot shows that without the endothermic effect there would be almost 10% greater mole fraction of hydrogen

Finally, Fig. 11 shows the effect of initial temperature of the driver gas and pressure ratio between driver and driven sections on molar fraction of hydrogen generated through the ammonia cracking process. Clearly, both parameters have positive influence on hydrogen production. Residence time between the reflected shock wave and the right running expansion fan ranges between 5.1 milliseconds at the highest pressure ratio and 5.4 milliseconds at the lowest pressure ratio. This indicates that the relationship shown in Fig. 11 is driven primarily by shock heating effects rather than residence time.

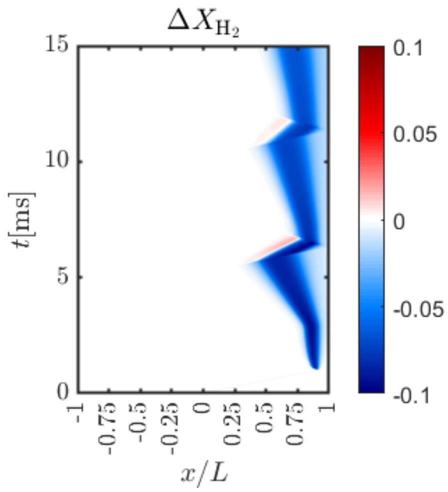

Figure 10: Change in hydrogen mole fraction due to endothermic effect.

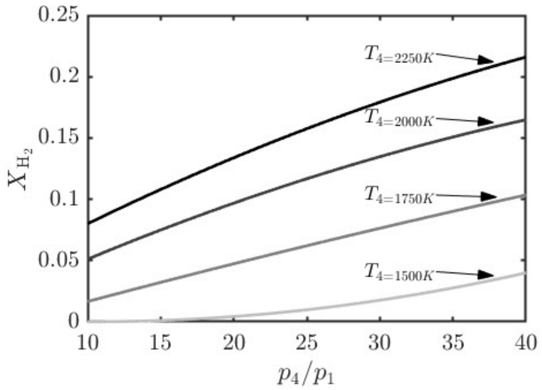

Figure 11: Hydrogen molar fraction as a function of pressure ratio between driver and driven sections and initial temperature of the driver gas.

III. Wave Reformer Description

The wave rotor is a direct energy-exchange device that utilizes one-dimensional pressure wave action for the transfer of mechanical energy between two compressible fluid flows which are at different pressure levels. Wave rotors are an established and experimentally verified technology [26-29]. A detailed historical review of wave rotor programs and their applications (until 2006) can be found in Ref. [30].

The wave rotor typically consists of a cylindrical rotor with a number of long axial channels arrange uniformly around its periphery. The rotor spins between two stationary endplates through which the flow enters and exists. Each endplate has a number of ports to accommodate the incoming and outgoing fluids. Each of the rotating channels operates similar to an individual shock tube. The entry and exit endplates function as the valves and resemble the shock tube diaphragm rupture, initiating a series of unsteady compression and expansion waves in the channels as they periodically rotate past the inlet and exit ports and regions of closed endplates. To generate compression waves, the channels are exposed to a high-pressure port of a driver gas which enters the channels and compresses the gas within it. To generate expansion waves, the channels are exposed to a low-pressure port and the gas in the channels discharges. By using a large number of channels on the rotating drum, the pulsed process occurring in a single shock tube is translated to a continuous process [26]. Therefore, the wave rotor can be considered the steady-flow, cyclical analogue of the pulsed shock tube. In a typical design, the channels are designed axially and arranged parallel to the drive shaft driven by a motor. In such a configuration, the only power input to the rotor is that necessary to overcome bearing friction. However, if the tubes are not axial (e.g. curved channels), net power can even be extracted from the rotor similar to that of a turbine in addition to the work exchange between the fluid streams [23].

A schematic of a typical wave rotor is shown in Fig. 12. Here, a high-pressure driver gas exchanges its energy with a low-pressure driven gas within the rotating channels. The figure shows the two stationary endplates (green and red colors) each of which has a few ports or manifolds that control the fluid flow through the channels. Between the rotor and the endplates faces there is no contact, but to minimize leakage, the gap is kept very small, or the endplates are built with sealing material that contact the rotor.

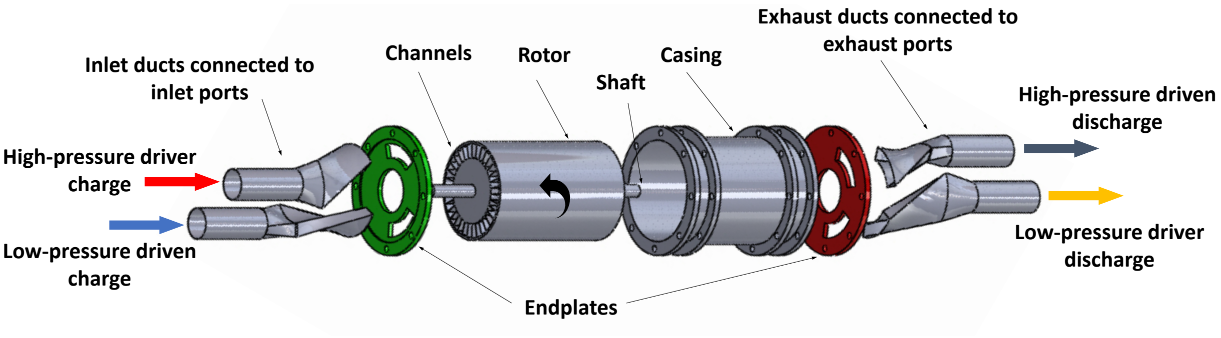

Figure 12: Schematic of a four-port wave rotor.

The wave rotor configuration shown in Fig. 12 uses two inlet ports and two outlet ports and thus, it can be referred to as a four-port wave rotor. The driven (low-pressure fluid) enters the rotor from an inlet port at one end of the rotor and after it is compressed it leaves at the opposite end of the rotor as a high-pressure driven gas using an outlet port (labeled “high-pressure driven gas.”). A driver fluid (high-pressure fluid) enters and leaves at the opposite end of the rotor as a low-pressure driver gas. Thus, the rotor experiences a through-flow pattern internally. The driver fluid expanded by expansion waves leaves the rotor at a pressure lower than that at which it came in. Thus, the energy gain in the driven gas is made up by a corresponding energy loss in the driver gas. By carefully selecting port locations and their widths, a significant and efficient transfer of energy can be obtained between flows in the connected ducts with minimum mixing between flows. The generated waves replace energy-exchange processes conventionally accomplished with compressors and turbines.

Figure 13 illustrates a wave reformer configuration using a four-port wave rotor architecture for ammonia pyrolysis. The device uses burned gas leaving a burner at a high pressure (driver gas) connected to the rotor by an inlet port. This incoming high-pressure gas compresses the preheated ammonia (driven gas) entering the rotor channels from a secondary inlet port. Due to the pressure difference between the driver and driven gases, a shock wave is generated in the channels. This transfers the driver gas energy to the driven ammonia gas. Under appropriate conditions, the temperature rise from the supersonic shock-wave compression heats up the driven ammonia gas to a temperature sufficient to thermally crack ammonia into hydrogen and nitrogen. The high-pressure products and expanded, driver gas separately exit the rotor from two exit ports as the labels demonstrate. It is helpful to note that the rotor channels are alternately exposed to relatively cooler driven gas at high frequencies; thus, the metal temperature of the rotor is expected to remain at a mean temperature significantly lower than the burned (post-combustor) gas temperature during the ammonia thermal decomposition.

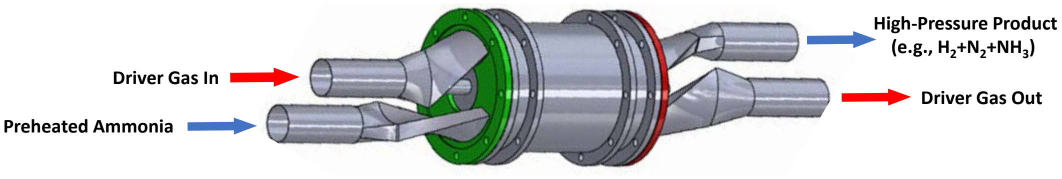

Figure 13: Schematic of a through-flow four-port wave reformer.

In the four-port wave rotor shown in Figs. 12 and 13, the inlet ports are located on one side of the rotor, and the outlet ports are located on the other. This is often known as a through-flow configuration. Alternatively, it is possible to design a reverse-flow device where each gas stream enters and leaves the channel from the same end. These two configurations may provide similar overall performance, but they differ substantially in their internal processes. Figure 14 shows a reverse-flow wave reformer.

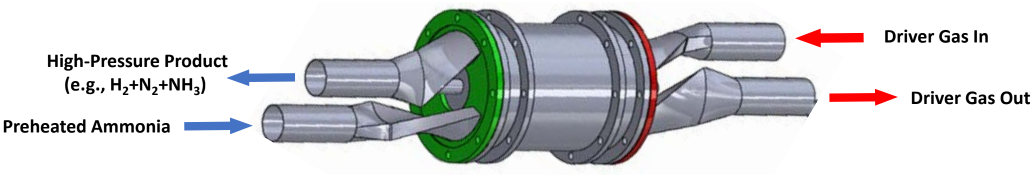

Figure 14: Schematic of a reverse-flow four-port wave reformer.

A. Inner Working Principles of a Through-Flow Wave Reformer

To better understand how a wave reformer operates, it is useful to investigate the physical phenomena occurring in the channels. This is traditionally studied by unrolling the rotor channels in a time-distance domain, often termed the 'wave diagram'. Figure 15 schematically illustrates an unwrapped through-flow reformer (shown in Fig. 13) with the rotor channel moving upward. In this fashion, the circular motion of the rotor channels is represented by straight translatory motion. The wave diagram portrays the position of the ports, the wave fronts, and the gas interfaces during each phase of the cycle, which is useful for visualizing the processes that occur in a single cycle of a wave machine. In the wave diagram, the horizontal axis represents the rotor axial length and the vertical axis is time (or rotational angle). The top of each wave diagram is looped around and joined to the bottom of the diagram since the journey of a channel of the wave rotor is periodic. The vertical black rectangles on each side of the diagram represents temporal locations of an endplate during which the inlet and outlet ports are closed. The diagonal lines are either the propagation lines (trajectories) of the waves or contact surface boundaries between the fluids (as labelled). In Fig. 15, the blue or lighter gray area represents the driven or reacting gas (ammonia) and the red or darker gray area represents the driver gas. Each cycle employs two inflow ports where ingress of the fresh, high-pressure driver and reacting fluids are fed into the moving channels, and two outflow ports where high-pressure fuel product and deenergized driver gas are discharged from the rotor channels. In the proposed cycle where the reacting gas is chosen to

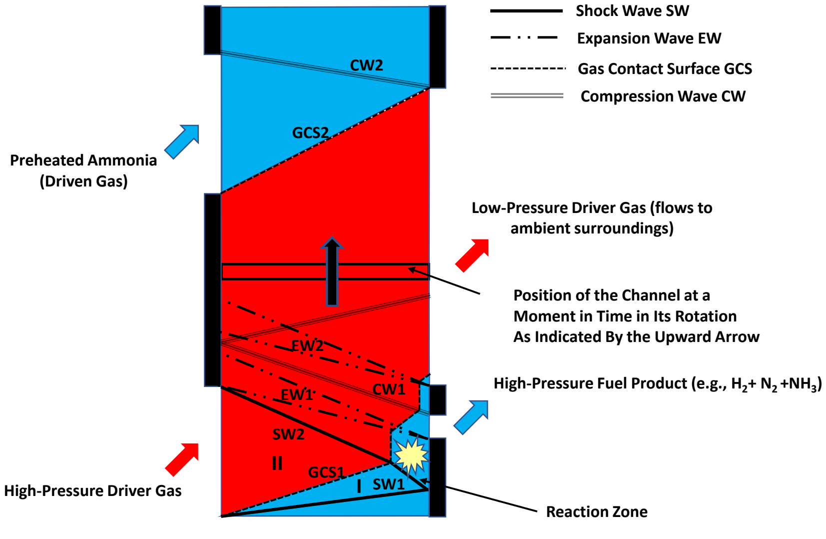

Figure 15: Wave diagram of a through-flow wave reformer.

be preheated ammonia, a mixture of ammonia and hydrogen is formed and extracted as a high-pressure fuel product leaving the rotor channels. In the following, the events occurring in a channel during one complete cycle will be described and it will be described in detail how shock and expansion waves are neatly employed to transfer the energy directly between the gases and generate hydrogen in the wave reformer.

Each cycle consists of two processes: a high-pressure part and a low-pressure part. The purpose of the former is to compress and heat up ammonia and deliver it to a combustion chamber. The latter is devised to discharge the burned gas, cool and fill the channel with a through-flow of fresh ammonia again.

In Fig. 15, the high-pressure part of the cycle begins at the bottom of the wave diagram where the flow within the channel is entirely filled with the low-pressure driven gas (ammonia). At this instance, the end ports are closed and the driver gas entry port (left side of diagram) suddenly opens. When the driver gas port opens, the high-pressure driver (burned gas from the burner) enters the channel and a primary shock wave (SW1) is generated that travels into the channel. SW1 travels rightward (solid line), compressing the driven gas. SW1 runs through the channel at a speed faster than the speed of sound and causes an abrupt rise of pressure. Behind the wave is the gas contact surface (GCS1) separating the driver gas (red/darker area, region II) from the compressed driven gas (blue/lighter color, region I) represented by a dotted line. This contact surface GCS1 follows SW1 to the right but at a rate that is slower than the shock wave. SW1 arrives at the right end of the channel and is reflected from an end wall. The reflected shock wave (SW2) propagates toward the left, further increasing the temperature of driver gas by converting the kinetic energy into heat in the reflection (or reaction) zone behind the wave. This immediately initiates pyrolysis of the reactant gas. SW2 continues propagating to the channel's left end, stopping the motion of the doubly compressed driven gas and the driver gas. This is indicated by turning the contact surface GCS1 into a vertical line. The peak temperature in the reaction zone is a function of the initial temperature of the reacting gas and the Mach number of the primary shock wave, SW1. With sufficient compression by the primary (SW1) and reflected (SW2) shock waves, the peak temperature, and consequently the thermal dissociation of ammonia to hydrogen, occurs in the reflection (or reaction) zone (yellow mark) prior to opening the exit port for exhausting the high-pressure fuel product. The reaction zone is maintained until the opening of the exit port. When the right end of the channel opens (i.e., outlet port for exhausting the high pressures fuel product), an expansion wave (EW1) is generated from the lower corner of the exit port, propagating to the left (dashed-dotted line). EW1 expands and expels the decomposed gas to the exit port, heading to the burner. Closing of the driver gas inlet port is timed with the arrival of EW1 front to the channel left end. Meanwhile, by closing the high-pressures fuel product exit port, a very small amount of ammonia will be retained in the channel and a compression wave (CW1) is generated from the upper corner of the exit port propagating to the left (doubled solid line) and stopping the channel flow. This is the end of the high-pressure part. At this moment, the fluid trapped in the channel consists primarily of burned gas and a small portion of the doubly compressed ammonia, preventing the hot gas from reaching the outlet port or contacting the right end wall.

The low-pressure part of the cycle starts when the entire driver gas is discharged by opening the exhaust-gas port, thereby generating another expansion wave (EW2) from the leading corner of the exhaust port. By opening the driven gas entry port, the pre-heated ammonia enters the channel while the expanded burned gas is leaving the channel from right, i.e., an overlap process. The two gases are separated from each other by a contact surface (GCS2). While the overlap process continues, the scavenging of gas through the exit port is stopped by closing the exhaust port. The closing of the exhaust port is timed with the arrival of the driven gas to the right end of the channel. Closing the exhaust port generates another compression wave (CW2) propagating to the left, stopping the flow of ammonia and increasing its pressure and temperature slightly. When CW2 meets the upper corner of the inlet port, the port closes, leaving the channel fully filled with ammonia and the next cycle can be initiated.

B. Inner Working Principles of a Reverse-Flow Wave Reformer

It is also possible to decompose the reactant gas in a different wave cycle introduced as the reverse-flow cycle. The ammonia pyrolysis is again achieved through shock compression by both incident and reflected shock waves, similar to that described in Fig. 15, but here the reactant fuel (ammonia) and processed fuel enter and leave from the left endplate. This is illustrated in Fig. 16. Likewise, the high-pressure and expanded driver gases enter and leave from the right endplate, as described in Fig. 14.

It is important to acknowledge that to achieve maximum yield of hydrogen during ammonia decomposition in the reaction zone, the peak temperature and residence time need to extend to their maximum values. In practice, the peak temperature in the reaction zone decreases because the ammonia-pyrolysis reaction is endothermic, with energy consumed and temperature decreasing as the reaction proceeds. Thus, at a lower temperature, a longer residence time is required to achieve high ammonia conversion. Ideally, this reaction time can be changed by adjusting the rotor speed, the rotor length, and port conditions. However, the rotor speed and the position and width of the ports are already set by the speed of the propagating waves to avoid undesired flow phenomena in the device, leading to a favorable, well-tuned wave pattern [31]. Therefore, it is beneficial to increase the residence time by allowing the processed gas to remain longer in the channel instead of expanding the gas quickly. NWH$_2$ has developed several reformer designs [14] that produce alternative wave cycles promoting longer residence time for a higher fuel-to-hydrogen conversion.

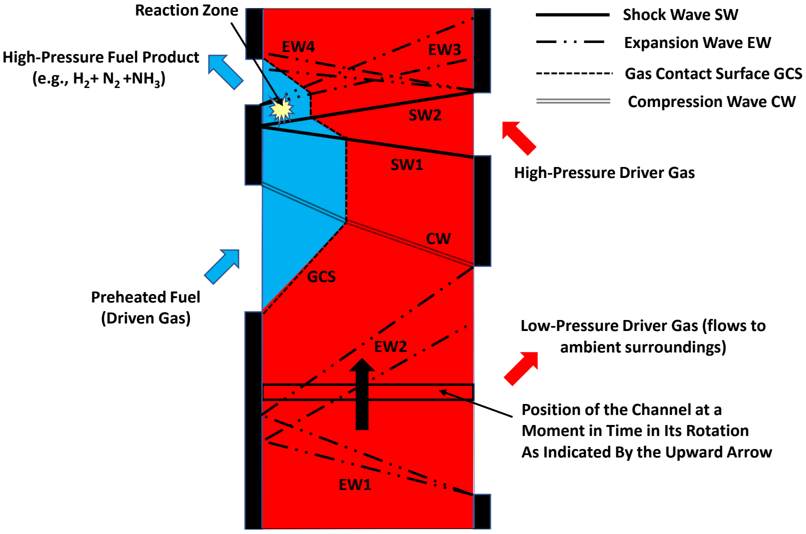

Figure 16: Wave diagram of a reverse-flow wave reformer.

IV. Application: Jet Engine

In this section, it will be described how the through-flow wave reformer can be adapted for cracking ammonia into a hydrogen gas mixture for obtaining sustainable aviation turbine power. First, it is envisioned that pure liquid ammonia is stored in the airplane fuel tank as a fuel. The fuel is then reformed or cracked by a shock wave reformer to produce ammonia/hydrogen blends in the engine. Note that this section is intended to provide the reader with a preliminary test-case of the concept that is first being reported in this work. This is not intended to provide an exhaustive analysis across different applications or flight conditions, but merely an indicative example of the viability of performing on-board ammonia reforming using a wave rotor.

A conceptual diagram of the system to reform ammonia to hydrogen in a jet engine is illustrated in Fig. 17. In this proposed arrangement, a typical inlet (diffuser) decelerates the incoming air (State a). The low-speed air enters a compressor (State 0) where its pressure is increased by the compressor blades. The compressed air is directed to a burner or combustor (State 1) where it is mixed with the fuel injected into the combustor. After the combustion process, the high-pressure burned gas splits into two lines and a small portion of it is delivered to the wave reformer (State 2) through the opening of the first port of the reformer. It must be kept in mind that bleeding gas from the combustor to the wave reformer would reduce the power produced in the turbine, thus, the amount of hot gas bled from the combustor should be as low as possible. The combustor gas bleed is used to compress preheated ammonia, residing in the channels, that has entered from a second port of the reformer (State 6). The incoming high-pressure gas (driver gas) triggers a shock wave in the rotor channel, which compresses the ammonia (driven gas) within the rotating channels. Such a shock compression can amplify the temperature of the ammonia high enough for thermal decomposition to take place, yielding a product mixture of primarily ammonia, hydrogen, and nitrogen. After the wave rotor spins and the channel aligns with a third port in the end plate, the channel end opens, and the produced blend of hydrogen, ammonia, and nitrogen. This fuel mixture is injected into the combustor (State 7). After further rotation of the channels, the fourth port opens and trapped, burned gas within the channels expands and flows to the surroundings (State 3). Alternatively, it is possible to use a heat exchanger to preheat the compressed air at State 1 before it enters the combustor, using the low-pressure, burned gas at State 3 (not shown). The efficacy of recovery this heat in State 3 will depend on its temperature and the percentage bleed flow required for the application.

The remaining (majority) of the high-pressure burned gas is delivered to the engine turbine (State 4). After work extraction in the turbine, the exhaust gas from the turbine exits the system (State 5). The exhaust gas enters a conventional heat exchanger that heats up the liquid ammonia entering the heat exchanger from a fuel tank (State 6′). The liquid ammonia vaporizes across the heat exchanger and is directed to the second port of the wave rotor (State 6). The cooled exhaust gas leaving the heat exchange enters a nozzle (State 5′) where it is accelerated and exhausted to the surroundings (State 8), producing the engine thrust in the case of aircraft engine. Here, in this novel system arrangement, the wave reformer provides zero-carbon fuel for the combustor using the energy contained in the burned gas. This arrangement could enhance the combustion process and it is a new application of wave rotors in propulsion systems, where the production of a dual-fuel blend of hydrogen and ammonia fuel is an integrated part of the aircraft engine.

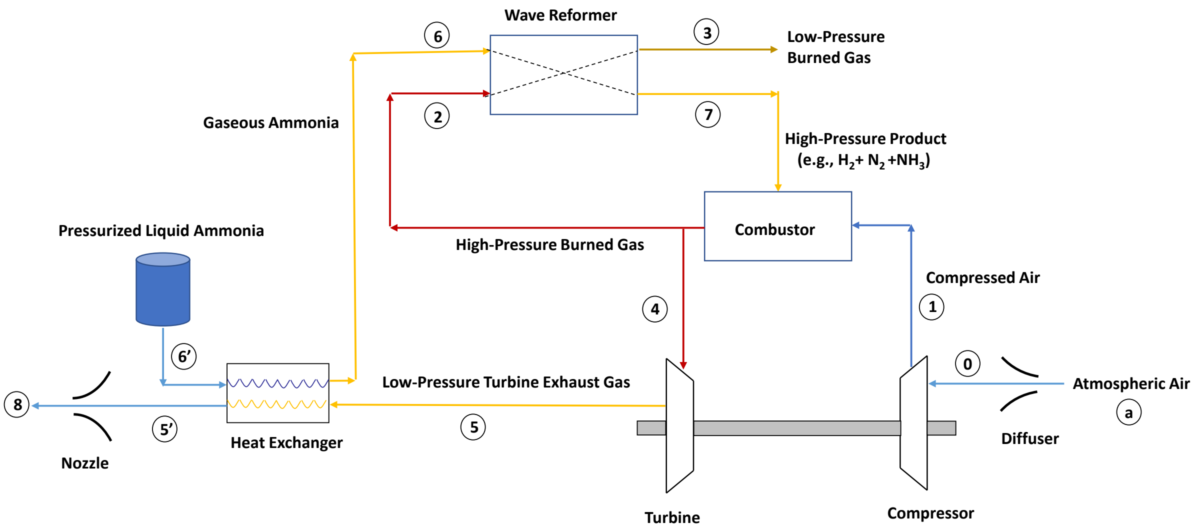

Figure 17: Schematic of a jet engine using a dual-fuel mixture of ammonia and hydrogen produced using a wave reformer.

To predict flow properties in and out of the wave reformer, it is required to conduct mass and energy balance calculations for an example engine application. A take-off condition of standard atmosphere, sea level was chosen as the design point. The design parameters of the baseline engine selected for this study include a compressor pressure ratio of 39, turbine total inlet temperature of 1830 K, and air flow rate of 1200 kg/s. A compressor isentropic efficiency of 87% was assumed for the compressor. Note the purpose of this example is not to propose a definitive implementation of this concept, but simply to use a case study with representative boundary conditions to conduct a preliminary wave rotor reformer analysis.

Figure 18 represents a numerical modeling of a wave reformer using the baseline engine. For this specific design, the rotor length is considered 0.5 m rotating at 7000 RPM. The channel height and width of each channel is selected as 8.5 cm and 5.7 cm, respectively. The port numbers (2, 3, 6, 7) correspond to those used in Fig. 17. The contour plots show pressure, temperature, Mach number, and velocity as a function of time or azimuthal position (vertical axis) and position (horizontal) over one complete cycle of operation. A color scale bar is provided to the immediate right of each contour plot. Axial distance is non-dimensionalised by channel length, L, and azimuthal position is represented by angular displacement, θ, and is non-dimensionalised by maximum angular displacement, $\theta_{\max}$, which corresponds to one full rotation of 360 degrees. To facilitate the detection of shock and expansion waves, the pressure contours are shown on a logarithmic scale. The velocity contours indicate flow in positive x-direction in red and flow along the negative x-axis in blue. This highlights where undesired backflow regions occur and can guide adjustment of the port timing accordingly.

The flow field contours are accompanied by the species contours in Fig.19 outlining the distribution of reactants (NH_3) and products (N_2 and H_2) expressed by the mole fraction X. Starting from the pressure plot, the wave reformer cycle can roughly be divided into a high-pressure zone starting at $\theta/\theta_{\max} = 0$ until approximately $\theta/\theta_{\max} = 0.4–0.5$ and is followed by a low-pressure zone for the remainder of the cycle until $\theta/\theta_{\max} = 1$. The high-pressure zone is dominated by a shock wave system consisting of an incident and a reflected shock wave, which account for peak pressures and temperatures within the cycle. In addition to the incident/reflected shock wave system, the plots also show a relatively weak shock wave is generated upon closure of port 3 to the channel. This left travelling wave collides with the stronger incident shock wave forming a colliding shock wave pattern. In the wake of this, the induced supersonic flow is slowed down to near sonic and subsonic conditions, the static pressure increased as a consequence and the static temperature in the driver gas raised by approximately 100 K.

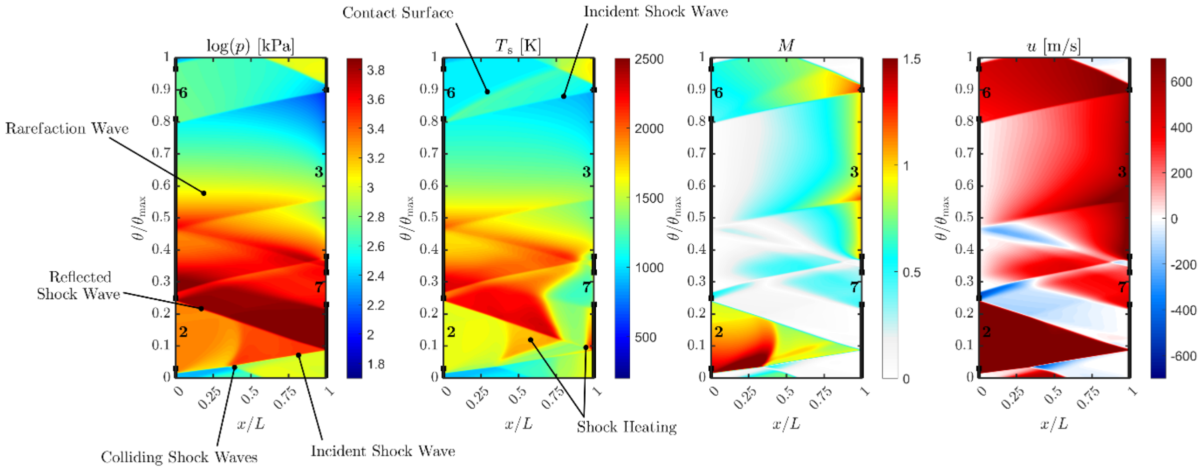

Figure 18: Contours of pressure plotted in logarithmic scale, temperature, Mach number and velocity in a four-port through-flow wave reformer.

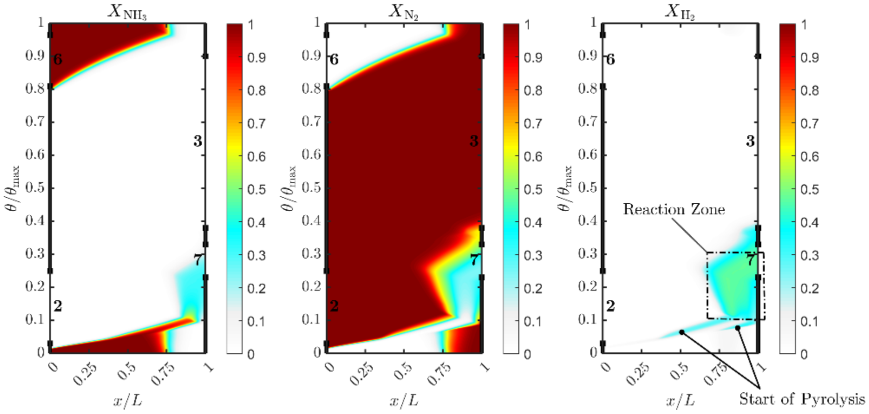

Figure 19: Species contour plots showing mole fraction of ammonia (NH_3), nitrogen (N_2) and hydrogen (H_2).

The mole fraction plots of the reactant and product species in Fig. 19 show that - in contrast to the shock tube simulations – the colliding shock waves initiate thermal decomposition of the incoming driven gas along the contact surface to the driver gas where driver and driven gas mix. This takes place approximately 0.30 millisecond prior to the incident shock wave is reflected from the right endplate and the outline reaction zone. Only upon exposure to the reflected shock wave the center portion of the ammonia stream with the highest concentration starts to decompose into its products. Overall, the gas mixture remains in the main reaction zone for around 1.0 millisecond. Downstream of the reflected shock wave, the peak temperature is approximately 800 K lower than in the rest of the channel to the left, where higher temperature driver gas dominates. This temperature difference is a combination of two factors; first and foremost, the driven gas enters the channel at approximately 1000 K and thus at considerably lower temperature compared to the driver gas, where static inlet temperatures range at around 1600 K. Secondly, the reaction taking place within the reaction zone is endothermic in nature, as shown in the shock tube tests, and further drives the temperature difference across the channel, effectively slowing the reaction down.

The high-pressure process generated by the shock wave system between ports 2 and 7 is then gradually expanded by the low-pressure port 3. A sufficiently long port width ensures the pressure within the channel can decrease in time for the low-pressure inlet at port 6 to inject the driven gas into the channel. In general, the greater the residual pressure within the channel, the greater the required inlet pressure for the driven gas to reach a desired penetration length becomes. In the shown example, the ammonia driven gas reaches approximately x/L=0.75 into the channel. From the temperature and Mach number plots, a discernable contact surface and a (weak) shock wave are visible.

To examine the effect of the driven gas inlet pressure, the mass flow split between driver and driven inlet mass flow rates is defined as:

$$\lambda = \frac{\dot{m}_2}{\dot{m}_6} \tag{9}$$

which can be directly linked to the penetration length into the channel and the required driven inlet pressure. The plots exhibited in Figs. 18 and 19 denote the flow field for a value of $\lambda = 10$. Figure 20 presents pressure, temperature and species mole fractions for two limiting cases of λ=2.5 and λ=30, respectively.

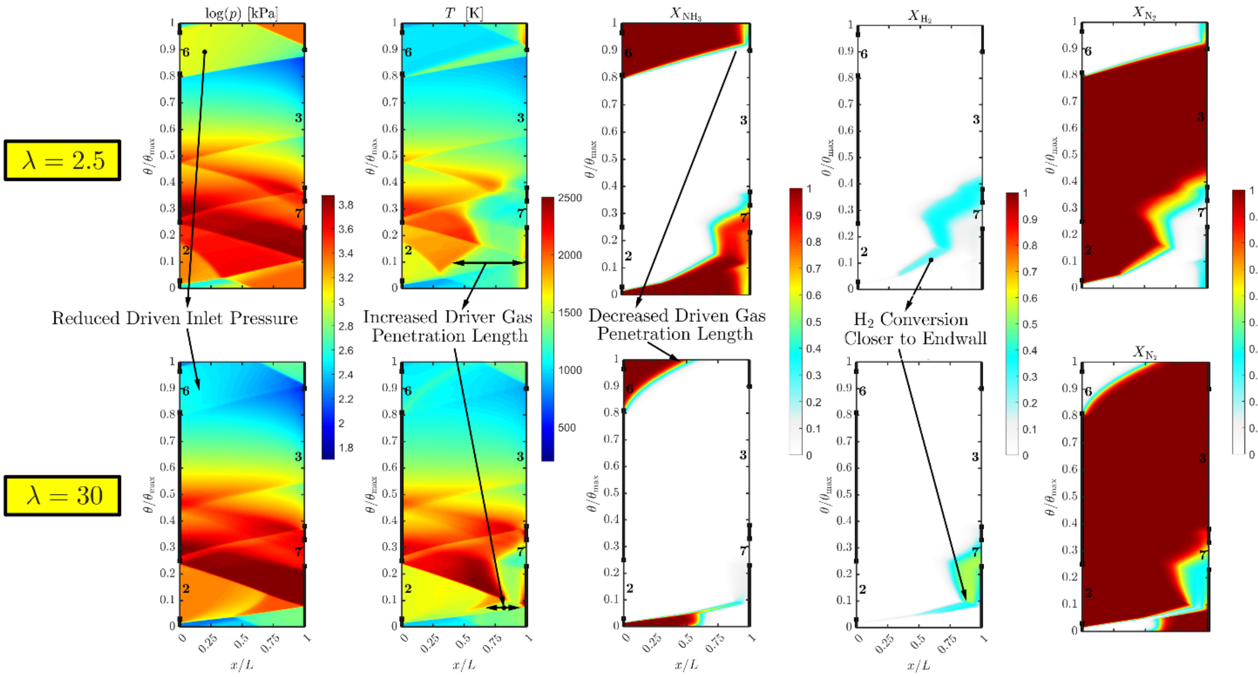

Figure 20: Flow field comparison between two different inlet mass flow splits λ.

For fixed driver inlet conditions, a decreasing λ requires an increased driven inlet pressure to match the required mass flow rate. This can be seen in the pressure distribution around the opening of the channel to port 6. In concert with the increased inlet pressure, the driven gas exhibits a greater penetration length into the channel, as indicated by the NH_3 species contour. In the shown example the driven gas covers well above 90% of the total channel length by the time port 6 closes for λ=2.5. This decreases considerably to approximately 50% for λ=30. As a consequence of the increased channel pressure downstream of port 6, the pressure ratio between port 2 and average channel pressure at $\theta/\theta_{max} = 0$ decreases and results in significantly reduced penetration length of the driver gases into the channel. Consistent with the previous examples, at λ=10 and the shock tube tests, the high-temperature driver initiates the conversion to H_2 at the contact surface. However, the lower the flow ratio, the more the start of conversion shifts towards the left and the inlet side of the reformer. This has significant consequences for the H_2 content in the outlet stream through port 7. As shown, in the mole fraction contours of Fig. 20, an excessive reduction in the mass flow ratio yields increased blockage to the driver port flow effectively depriving it of the means to direct the driven gas well into the target reaction zone and subsequently out of the reformer through port 7.

This can be summarized by plotting the cycle-averaged mole fraction of H_2 through the high-pressure exhaust port 7 against the flow ratio λ, as done in Fig. 21. It becomes clear that the H_2 content in the stream of port 7 experiences an initially linear increase with flow ratio before reaching a plateau at approximately 47.6%. Since the flow ratio also has an influence on the percentage of post-combustion gas that is bled off to the wave rotor reformer, there may be a trade-off between cycle efficiency and ammonia conversion.

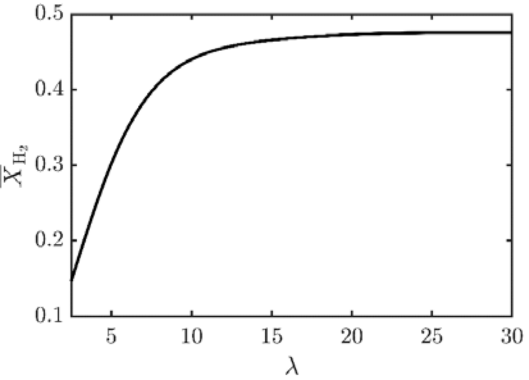

Figure 21: Variation of the average mole fraction in the high-pressure outlet stream through port 7 plotted against the inlet mass flow ratio λ.

The results of the calculations are shown in Table 1. For each state point at inlets and outlets of the wave reformer, the mass flow rate, static pressure, and static temperature are reported. Consistent with results observed in the wave diagrams, it is seen that by increasing λ, intake port pressure reduces (P_6). Additionally, a reduction of NH_3 penetration length and an increase in the N_2 penetration length in the channel characterized by $\dot{m}_6$ and $\dot{m}_2$ variations are seen.

Table 1: Calculated wave reformer port thermodynamic properties according to the state numbering in Fig. 17.

λ $\dot{m}_2/\dot{m}_6$	$\dot{m}_2$ (kg/s)	$\dot{m}_6$ (kg/s)	$\dot{m}_3$ (kg/s)	$\dot{m}_7$ (kg/s)	Bleed % $\dot{m}_2/(\dot{m}_1+\dot{m}_7)$	T_2 (K)	T_6 (K)	T_3 (K)	T_7 (K)	P_2 (kPa)	P_6 (kPa)	P_3 (kPa)	P_7 (kPa)
5	108.6	21.7	102.5	27.8	8.84	1600.4	1028.7	1258.8	1459.6	2193.2	805.8	101.3	2026.5
10	114.7	11.5	99.2	26.9	9.35	1601.6	1043.1	1344.4	1591.7	2188.9	557.7	101.3	2026.5
15	117.0	7.8	96.2	28.7	9.52	1602.6	1049.2	1393.7	1632.6	2194.1	455.0	101.3	2026.5
20	118.3	5.9	95.5	28.7	9.63	1603.2	1052.7	1422.5	1664.4	2197.1	400.8	101.3	2026.5
25	119.2	4.8	95.7	28.3	9.70	1603.0	1054.9	1442.7	1688.8	2197.3	367.5	101.3	2026.5

V. Conclusion

An innovative method for in-flight pyrolysis of ammonia to produce a zero-carbon fuel blend of ammonia and hydrogen for jet engines is described. The basis of the innovation is the wave rotor technology that uses shock (pressure) waves to exchange energy between two fluids in direct contact. The shock waves travel along channels arranged in an array around the circumference of the rotor. A reformer adopts a wave rotor to harnesses energy contained in the engine burner exhaust-gas to compress and heat gaseous ammonia until it partially decomposes and forms hydrogen and nitrogen. This process uses shock-wave heating to efficiently achieve the high temperatures required for ammonia cracking; it does not require any external heat source and instead utilizes a low percentage of the hot, high-pressure exhaust gas bled off from the burner. To investigate the potential of shock waves to heat up a gas to temperatures sufficiently high to initiate decomposition of ammonia, a single reaction model was developed and compared to a more detailed kinetic model - confirming good agreement for the residence time of interest. A shock tube study was then carried out that could highlight trends in shock compression and hydrogen formation in the driven section of the tube. Temperature rises above 3 times the initial value demonstrated sufficiently large shock heating for ammonia cracking. Incorporating the kinetic model demonstrated the influence of the initial temperature of the driver gas and pressure ratio between driver and driven sections on hydrogen production. Shifting focus to a four-port wave rotor integrated into an aviation engine, it was found that hydrogen was also formed in the channels of the reformer through cracking of onboard ammonia as fuel. The simulation demonstrated it is possible to achieve significant rates of ammonia thermal dissociation that varied in relation to the mass flow split between driver and driven inlet. In conclusion, this work demonstrated the viability of utilizing a shock wave reformer to achieve substantial rates of ammonia-hydrogen conversion. Future work should include expanding this concept to encompass a range of different applications and cycle conditions. In addition, more detailed modelling of the complete system is needed to research system-level optimization and combustion modelling.

Acknowledgments

The authors would like to thank and acknowledge the co-funding for this and ongoing work from Emissions Reduction Alberta (ERA), the Natural Gas Innovation Fund (NGIF), and GRTgaz.

References

[1] Siddiqui, O., and Dincer, I., "A Comparative Life Cycle Assessment of Clean Aviation Fuels," *Energy*, Vol. 234, 2021, pp. 121126.

[2] Khandelwal, B., Karakurt, A., Sekaran, P. R., Sethi, V., and Singh, R., "Hydrogen Powered Aircraft: The Future of Air Transport," *Progress in Aerospace Sciences*, Vol. 60, 2013, pp. 45-59.

[3] Nojoumi, H., Dincer, I., and Naterer, G. F., "Greenhouse Gas Emissions Assessment of Hydrogen and Kerosene-Fueled Aircraft Propulsion," *International Journal of Hydrogen Energy*, Vol. 34, Issue 3, 2009, pp. 1363-1369.

[4] Valera-Medina, A., Xiao, H., Owen-Jones, M., David, W. I. F., and Bowen, P. J., "Ammonia for Power," *Progress in Energy and Combustion Science*, Vol. 69, pp. 2018, 63–102.

[5] Kobayashi, H., Hayakawa, A., K. D., Somarathne, A., and Okafor, E. C., "Science and Technology of Ammonia Combustion," *Proceedings of the Combustion Institute*, Vol. 37, Issue 1, 2019, pp: 109-133.

[6] Li, J., Huang, H., Kobayashi, N., He, Z., and Nagai Y., "Study on Using Hydrogen and Ammonia as Fuels: Combustion Characteristics and NO_x Formation," *International Journal of energy Research*, Vol 38, No. 9, 2014, pp: 1214-23

[7] Balestri, M., Cecchini, D., and Cinci, V., "Unconventional Fuels Experimental Campaigns in Gas Turbine Combustor at ENEL Sesta Facility," ASME Paper GT2004-53274, 2004.

[8] Karabeyoglu, A., Brian, E, Stevens, J., and Cantwell, B., "Development of Ammonia Based Fuels for Environmentally Friendly Power Generation," *10th International Energy Conversion Engineering Conference*, 2012.

[9] Kurata, O., Iki., N., Matsunuma, T., Inoue, T., et al., "Success of Ammonia-Fired, Regenerator-Heated, Diffusion Combustion Gas Turbine Power Generation and Prospect of Low NOx Combustion with High Combustion Efficiency," ASME Paper POWER-ICOPE2017-3277, 2017.

[10] Xiao, H., and Valera-Medina, A., "Chemical Kinetic Mechanism Study on Premixed Combustion of Ammonia/Hydrogen Fuels for Gas Turbine Use," *ASME Journal of Engineering for Gas Turbines and Power*, Vol. 139, No. 8, 2017, pp: 081504.

[11] Taussig, R. T., "Wave Rotor Turbofan Engines for Aircraft," Winter Annual Meeting of the ASME, edited by Sladky, J. F., *Machinery for Direct Fluid-Fluid Energy Exchange*, AD-07, 1984, pp. 9-45.

[12] Taussig, R., Cassady, P., Zumdieck, J., Thayer, W. and Klosterman, E., "Investigation of Wave Rotor Turbofans for Cruise Missile Engines," Final Report Submitted by MSNW to DARPA, Contract No. N00140-82-C-9729, 1983.

[13] Kielb, R., "Hydrocarbon Waver Reformer and Methods of Use," US Patent Application 20180215615, 2018.

[14] Akbari, P., Copeland, C. D., Tüchler, S., Davidson, M., and Mahmoodi-Jezeh, S. V., "Shock Wave Heating: A Novel Method for Low-Cost Hydrogen Production" ASME Paper IMECE2021-69775, 2021.

[15] Alturaifi, S. A., Mathieu, O., and Petersen, E. L., "An Experimental and Modeling Study of Ammonia Pyrolysis," *Combustion and Flame*, 2021.

[16] Davidson, D. F., Kohse-Höinghaus, K., Chang, A. Y., and Hanson, R. K., "A Pyrolysis Mechanism for Ammonia," *International Journal of Chemical Kinetics*, Vol. 22, 1990, pp. 513–535.

[17] Kohse-Höinghaus, K., Davidson, D. F., Chang, A. Y., and Hanson, R. K. "Quantitative NH2 Concentration Determination in Shock Tube Laser-Absorption Experiments," *Journal of Quantitative Spectroscopy and Radiative Transfer*, Vol. 42, No. 1, 1989, pp. 1–17.

[18] Miyama, H., and Endoh, R., "Ignition of Ammonia-Air Mixtures by Reflected Shock Waves," *Combustion and Flame*, Vol. 11, Issue 4, 1967, pp: 359-360.

[19] Drummond, L. J., "High Temperature Oxidation of Ammonia," *Combustion Science and Technology*, Vol. 5, Issue 1, 1967, pp: 175-182.

[20] Shu, B., Vallabhuni, S. K., He, X., Issayev, G., et al., "A Shock Tube and Modeling Study on the Autoignition Properties of Ammonia at Intermediate Temperatures," *Proceedings of the Combustion Institute*, Vol. 37, 2019, pp: 205–211.

[21] Glarborg, P., Miller, J. A., Ruscic, B., and Klippenstein, S. J., "Modeling Nitrogen Chemistry in Combustion," *Progress in Energy and Combustion Science*, Vol. 67, 2018, pp: 31–68.

[22] Chemkin Pro 15172, Reaction Design, 2016.

[23] Tüchler, S., and Copeland, C. D., "Validation of a Numerical Quasi-One-Dimensional Model for Wave Rotor Turbines with Curved Channels," *ASME Journal of Engineering for Gas Turbines and Power*, Vol. 142, No. 2, 2020, pp: 021017.

[24] Tüchler, S., and Copeland, C. D., "Parametric Numerical Study on the Performance Characteristics of a Micro-Wave Rotor Gas Turbine," *International Gas Turbine Congress*, Paper IGTC-2019-200, 2019.

[25] Tüchler, S., and Copeland, C. D., "Experimental and Numerical Assessment of an Optimized, Non-Axial Wave Rotor Turbine," *Applied Energy*, Vol. 268, 2020, pp: 115013.

[26] Rose, P. H., "Potential Applications of Wave Machinery to Energy and Chemical Processes," *Proceedings of the 12th International Symposium on Shock Tubes and Waves*, 1979, pp. 3-30.

[27] Shreeve, R. P., and Mathur, A., *Proceeding of the 1985 ONR/NAVAIR Wave Rotor Research and Technology Workshop, Report NPS-67-85-008*, Naval Postgraduate School, Monterey, CA, 1985.

[28] Kentfield, J. A. C., "Wave Rotors and Highlights of Their Development," AIAA Paper 98-3248, 1998.

[29] Welch, G. E., “Overview of Wave-Rotor Technology for Gas Turbine Engine Topping Cycles,” *Novel Aero Propulsion Systems International Symposium, The Institution of Mechanical Engineers*, 2000, pp. 2-17.

[30] Akbari, P., Nalim, M. R., and Müller, N., “A Review of Wave Rotor Technology and Its Applications,” *ASME Journal of Engineering for Gas Turbines and Power*, Vol. 128, No. 4, 2006, pp. 717-735.

[31] Gyarmathy, G., “How Does the Comprex Pressure-Wave Supercharger Work?,” SAE Paper 830234, 1983.